Computers in Biology and Medicine 109 (2019) 43–52

Contents lists available at ScienceDirect

Computers in Biology and Medicine

journal homepage: www.elsevier.com/locate/compbiomed

Biomechanical performance of cranial implants with different thicknesses and material properties: A finite element study

Petr Marcián[a,*], Nathaniel Narra[b], Libor Borák[a], Jakub Chamrad[a], Jan Wolff[c,d]

[a] Institute of Solid Mechanics, Mechatronics and Biomechanics, Faculty of Mechanical Engineering, Brno University of Technology, Brno, Czech Republic
[b] Division of Biomedical Engineering, Department of Human Biology, Faculty of Health Sciences, University of Cape Town, Cape Town, South Africa
[c] Department of Oral and Maxillofacial Surgery, Division for Regenerative Orofacial Medicine, University Hospital Hamburg-Eppendorf, Hamburg, Germany
[d] Fraunhofer Research Institution for Additive Manufacturing Technologies IAPT, Hamburg, Germany

ARTICLE INFO

Keywords:
Cranioplasty
Skull implant
3D printing
Finite element method
Mechanical properties

ABSTRACT

This study investigated the effect of implant thickness and material on deformation and stress distribution within different components of cranial implant assemblies. Using the finite element method, two cranial implants, differing in size and shape, and thicknesses (1, 2, 3 and 4 mm, respectively), were simulated under three loading scenarios. The implant assembly model included the detailed geometries of the mini-plates and micro-screws and was simulated using a sub-modeling approach. Statistical assessments based on the Design of Experiment methodology and on multiple regression analysis revealed that peak stresses in the components are influenced primarily by implant thickness, while the effect of implant material is secondary. On the contrary, the implant deflection is influenced predominantly by implant material followed by implant thickness. The highest values of deformation under a 50 N load were observed in the thinnest (1 mm) Polymethyl Methacrylate implant (Small defect: 0.296 mm; Large defect: 0.390 mm). The thinnest Polymethyl Methacrylate and Polyether Ether Ketone implants also generated stresses in the implants that can potentially breach the materials' yield limit. In terms of stress distribution, the change of implant thickness had a more significant impact on the implant performance than the change of Young's modulus of the implant material. The results indicated that the stresses are concentrated in the locations of fixation; therefore, the detailed models of mini-plates and micro-screws implemented in the finite element simulation provided a better insight into the mechanical performance of the implant-skull system.

1. Introduction

A dramatic growth in 3D printing technology and its overall accessibility has revolutionized many fields such as manufacturing, education, healthcare to name a few [1]. In the field of medical implantology, cranioplasty has benefited from this technology by offering greater treatment options and improved quality [2,3]. Patient-specific skull implants manufactured using 3D printing technologies are gaining in popularity since they offer a unique possibility to improve treatment planning and implant design, which consequently influences the success of the therapy [4–7]. The current 3D printing workflow process comprises four basic steps: patient scanning, treatment design, implant fabrication, and implantation. The 3D printing workflow typically takes a few days with printing times of approximately 10 h [8].

The long-term stability and reliability of the aforementioned constructs is still not well documented mainly due to the infancy of the technology. There are numerous factors that can affect the long-term reliability: defect location, shape, bone quality, expected loads on the implant assembly, and constraints caused by the surrounding soft tissue and bony structures [9–11].

To date, only a few studies have simulated and assessed the role of implant shape, location, mechanical loading character, and implant-bone interface geometry [10–15]. This is especially important in patients with large cranial defects. Based on clinical and engineering experience, a biomechanical cranial implant performance related to such defects is mainly influenced by the following two factors: implant material and implant thickness. This influence shall be further investigated.

To date the most common biomaterials used for 3D printed skull implants are Polymethyl Methacrylate (PMMA), Polyether Ether Ketone (PEEK) and titanium alloy Ti6Al4V (α - β Titanium alloy) [16,17]. The implant thickness usually depends on the defect size and location which

* Corresponding author.
E-mail address: marcian@fme.vutbr.cz (P. Marcián).

https://doi.org/10.1016/j.compbiomed.2019.04.016
Received 8 November 2018; Received in revised form 18 April 2019; Accepted 18 April 2019

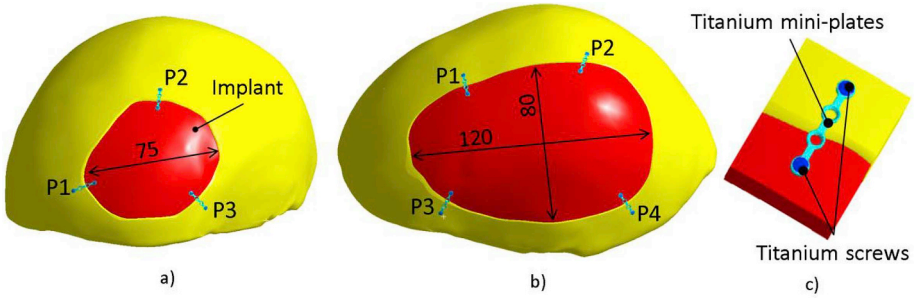

Fig. 1. Model geometry: a) Coarse model of smaller defect (circular shape, 2412 mm^2), b) Coarse model of larger defect (elliptical shape, 8030 mm^2), c) Sub-model.

can dictate the necessary functional rigidity. To the best of the authors' knowledge, there are currently no studies that provide an insight into how different implant materials and thicknesses affect the performance of cranial implants design and which of those two factors is more significant. In this study, the mechanical behavior of cranial implant assembly is studied as a function of varying thickness and material through a finite element based computational modeling approach and a statistical assessment. In order to provide a deeper insight into the cranial implant performance, the implant assembly is simulated including a detailed geometry of fixing the mini-plates and the micro-screws which are assumed to be significant components for correct evaluation of stress distribution within the implant.

2. Methods

An anatomically realistic model consisting of a human skull, cranial implant, mini-plates and micro-screws (Fig. 1) was constructed and studied using non-linear computational simulations based on the finite element (FE) method. A human cadaver skull was acquired from the Department of Anatomy, Faculty of Medicine, Masaryk University Brno, Czech Republic in full accordance with relevant institutional and legislative requirements. The skull was subsequently imaged using a computed-tomography scanner (General Electric v tome x L240, Boston, Massachusetts, USA). The resulting Digital Imaging and Communications in Medicine (DICOM) data was converted into a Standard Tessellation Language (STL) format file to acquire a 3D STL model of the skull [18]. All necessary image processing procedures were performed using STL Model Creator software (implemented in Matlab 2012, Math Works, Natick MA, USA) [19]. Two typical cranial defects [10] were subsequently artificially generated on the STL model of the skull. The first cranial defect was of circular shape with an area of 3412 mm^2, labeled as a smaller defect throughout this study (Fig. 1a). The second cranial defect was of elliptical shape with an area of 8030 mm^2, labeled as a larger defect throughout this study (Fig. 1b). The procedural details used for modeling were elaborated in previous studies by Ridwan-Pramana et al. [10,11]. The STL models of the smaller and larger skull defects were subsequently imported as solid objects in SolidWorks (Dassault Systems, Vélizy-Villacoublay, France). In SolidWorks, two cranial implants were virtually designed to perfectly fit the small and large defect sites. Four different cranial implant thicknesses were designed for each defect size: 1 mm, 2 mm, 3 mm, and 4 mm (Fig. 2). The implant thicknesses were labeled as T1, T2, T3 and T4. Mini-plates, and micro-screws required for cranial implant fixation were created using the same software. Finally, all components were assembled using a FE simulation tool in ANSYS® Academic Research Mechanical, Release 18.1 (Swanson Analysis, Inc. Houston, PA, USA) where all FE-related preparations and calculations were performed (Fig. 4). In total, three different skull implant materials were simulated: PMMA, PEEK and Ti6Al4V (Table 1).

The cranial implant was fixed to the skull using three (smaller defect) and four (larger defect) conventional mini-plates (KLS Martin, MICROPL., 1.0, 3-holes, 0.6 mm) and two micro-screws per mini-plate (∅ 1 mm, length 2 mm). The mini-plates were positioned according to

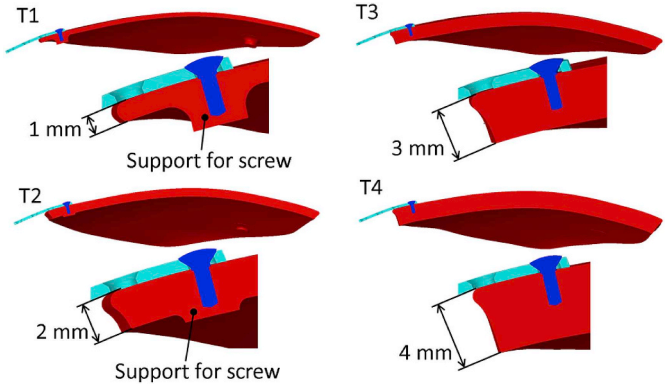

Fig. 2. Four different PMMA implant thicknesses.

Table 1
Material properties.

Material	Young's modulus [MPa]	Poisson's ratio [−]	Ref.	Yield strength [MPa]	Ref.
Bone	15 000	0.3	[20,21]	–	–
PMMA	3000	0.38	[22,23]	65	[24]
Ti6Al4V	110 000	0.3	[25]	825	[25]
PEEK	4000	0.38	[26]	110	[26]

the recommendations of an experienced surgeon in such a way that they were distributed evenly along the implant circumference and were oriented perpendicularly to the bone-implant interface [10]. The mini-plate positions were labeled P1, P2, P3 and P4 (Fig. 1, note that the position P4 applies only to the larger defect).

The following three loading scenarios were modeled for both defect sizes (Fig. 3):

1. Intracranial pressure of 15 mmHg [27] + external force of 5 kg [28] acting perpendicularly on the implant (labeled as "ICP + Force").
2. Intracranial pressure of 15 mmHg + external force of 5 kg acting at an angle of +45° through the center of the implant (labeled as "ICP + Force(+45)").
3. Intracranial pressure of 15 mmHg + external force of 5 kg acting at an angle of −45° through the center of the implant (labeled as "ICP + Force(-45)").

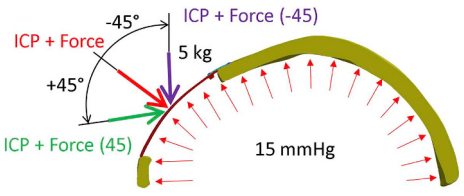

Fig. 3. Loading scenarios.

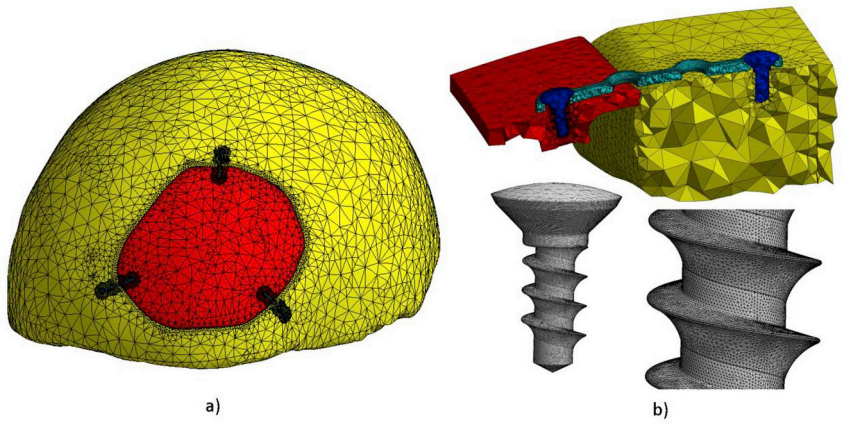

Fig. 4. FE mesh: a) Coarse model, b) Sub-models.

The mechanical performance of the bone-implant construct was analyzed in terms of two parameters: 1. Deformation; 2. Mechanical stress. The global implant deformation can be assessed using a relatively coarse FE mesh and excluding the specifics of the bone-implant interface. However, mechanical stress assessment of the micro-threaded connection requires a finer FE mesh of the screw model and of the region proximal to the fixation screw. Therefore, in order to minimize the overall computing time, a sub-modeling strategy [29–32] was employed and the analysis was performed in two stages:

1. *Coarse model* (Fig. 4a): A computational model of the entire implant assembly. The mini-plates were simplified by excluding the details such as fillets and chamfers, and the micro-screws were simplified by excluding the threads (i.e. idealized cylinders were used instead). The coarse model was fixed (boundary condition) at the bottom edge of the skull. In total, 72 configurations of the coarse model were simulated (Fig. 5). Directional displacements of the cranial implant (i.e. displacements in the transversal direction, UZ) were evaluated in each configuration. These displacements were evaluated at the center of the implants, i.e. in the point of the force application (Fig. 6).
2. *Sub-model* (Fig. 4b): The sub-model consisted of smaller regions of the skull and cranial implant (Fig. 1c) and of the mini-plates and micro-screws. The micro-screw on the implant side was modeled including a detailed (helical) micro-thread. All components of the sub-model were discretized by the FE meshes finer than those used in the coarse model. The sub-model was loaded by displacements applied on its boundary and at the same time by ICP. The boundary displacements were extracted from the corresponding coarse model [11]. In total, 252 configurations of the sub-model were analyzed (combinations of 2 defects, 3 implant materials, 4 thicknesses, 3 load cases, and 3 or 4 mini-plate positions, i.e. 3x4x3x3 + 3x4x3x4 = 252; see Fig. 5 for combinations illustration). The sub-model was analyzed for von Mises stresses in the implant body (especially in close vicinity of the threads), micro-screws and in the mini-plates.

The FE meshes of both computational model types (i.e. coarse model & sub-model) consisted of quadratic hexahedral and tetrahedral second order elements (Ansys elements SOLID186 and SOLID187). The smallest element size in the coarse model was 0.3 mm, the smallest element size in the sub-model was 0.003 mm. Element sizes were chosen based on the results of preliminary tests and sensitivity calculations. Element quality checks were subsequently performed. All parts were connected using contact elements TARGE160 and CONTA174 assuming a frictional option in all contact pairs except for the contacts between the simplified cylindrical screw and the implant/bone which were assumed to be bonded [11]. The total number of the elements ranged from 130 000 to 800 000 depending on the variant of the model.

Two different approaches were adopted to assess how the implant thickness and Young's modulus affect the implant mechanical performance and which of these two factors is more significant in terms of implant deformation and stress distribution within the assembly:

The first approach utilized a resemblance of the cranial implant with an ideal partially-spherical shell (see Appendix for more details). Transverse deflection of the latter can be calculated using Eq. (A.3). This equation shows that the maximum shell deflection is negatively correlated to the product of Young's modulus and thickness powered by exponents 1 and 2, respectively. However, as for the implant, there were certain deviations from the ideal partially-spherical shell;

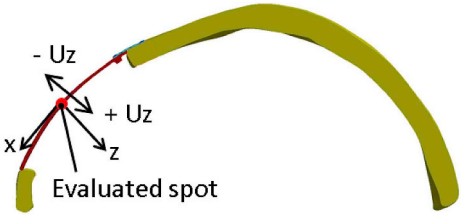

Fig. 6. Local coordinate system for directional displacement (UZ; transverse deflection) evaluation.

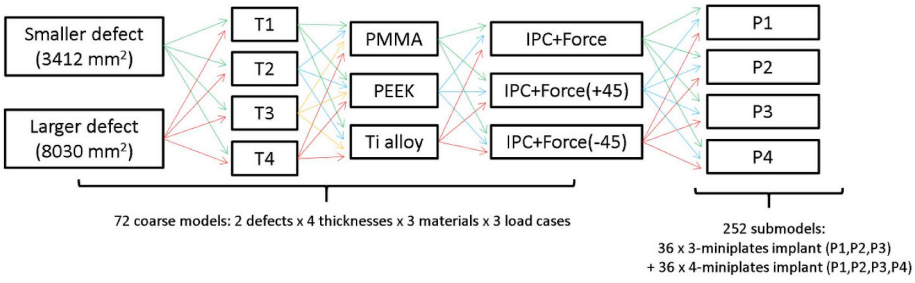

Fig. 5. All combinations of the implant thickness, material, and loading establish the variants of the computational model.

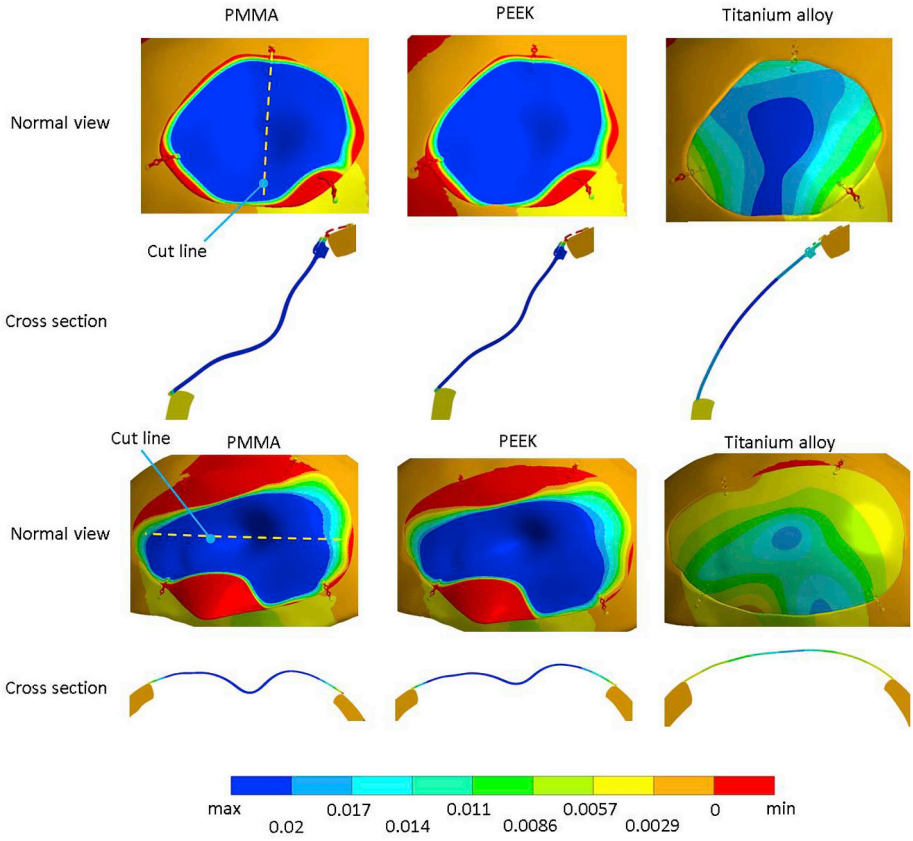

Fig. 7. Comparison of PMMA, PEEK and Titanium alloy implant (UZ) displacements [mm] in coarse model (scale: 50 times magnification), loaded by load case ICP + Force. T = 1 mm. Upper row: Smaller defect (3412 mm^2); Lower row: Larger defect (8030 mm^2).

therefore, Eq. (A.3) provides a less accurate approximation of this specific case. Assuming a similar negative correlation, a multiple linear regression analysis was performed to acquire a better approximation of Eq. (A.3). Based on the coarse model results (UZ), the maximum transverse deflection can be approximated by following power function:

$$w = \frac{M}{E^N . t^Q} \tag{1}$$

where M is a numerical coefficient that depends upon the overall geometry and loading, E is implant Young's modulus and t is implant thickness. Coefficient M and exponents N and Q are obtained from the multiple linear regression analysis. Assuming two levels of both factors (t_{min}, t_{max}, E_{min}, E_{max}), it can be easily proved that thickness has a stronger effect on the deflection than the Young's modulus if a ratio of Q/N is greater than a limit given by Eq. (2) (and vice versa):

$$\left(\frac{Q}{N}\right)_{limit} = log_{\frac{t_{max}}{t_{min}}} \frac{E_{max}}{E_{min}} \tag{2}$$

This approach is only applicable to the coarse model results.

The second approach utilized a more general statistical method and is applicable to the coarse model and sub-model. In order to investigate the effects of all different factors and their mutual interactions on the implant performance, all calculated results (i.e. displacements and stresses) were processed using the methodology of full factorial Design of Experiments (DOE) at two levels for four factors and the effects were assessed using a one-way analysis of variance (ANOVA). Specifically, the following factors and their extreme values, along with corresponding deflection or stress results, were used for the statistical assessment: Factor A: Implant Young's modulus {3000 MPa, 110000 MPa}, Factor B: Implant thickness {1 mm; 4 mm}, Factor C: Defect size {3412 mm^2; 8030 mm^2}, Factor D: Load direction {IPC + Force(-45); IPC + Force(+45)}. To secure the normal distribution of the input data, log-transformed data were used for the statistical assessment. A significance level of $\alpha = 0.05$ was assumed.

3. Results

3.1. Coarse model

Deformation of the implant is presented in Fig. 7, and the maximum values are summarized in Fig. 8. The highest UZ values 0.296 mm (smaller defect) and 0.390 mm (larger defect) were observed in the thinnest PMMA implant (T1) loaded by ICP + Force. As indicated in Fig. 8, the deformation magnitudes in the PMMA and PEEK implants were consistently greater than that of the Ti6Al4V implant with corresponding thickness in both implant sizes. In both polymer-based implants, the lowest deformation value (UZ) was observed in T4 and ranged (depending on the loading scenario) from 0.028 to 0.05 mm (smaller defect) and from 0.029 to 0.050 mm (larger defect). On the contrary, in the titanium alloy implant, the largest deformation was observed in T1 ranging 0.014–0.023 mm (smaller defect) and 0.019–0.029 mm (larger defect). Results of the multiple linear regression analysis are presented in Table 2. The DOE results are presented in Fig. 11a. Effects of all investigated factors and their interactions are represented by dots in Fig. 11a. Effects that fall near the line are considered to be insignificant, while those that are far from the line are further tested for statistical significance with ANOVA. Results of the test are summarized in Table 3.

3.2. Sub-model

Typical von Mises stress distributions in the individual components of the assembly (implant, mini-plates and micro-screws) for different thickness configurations are illustrated in Fig. 9. The maximum von

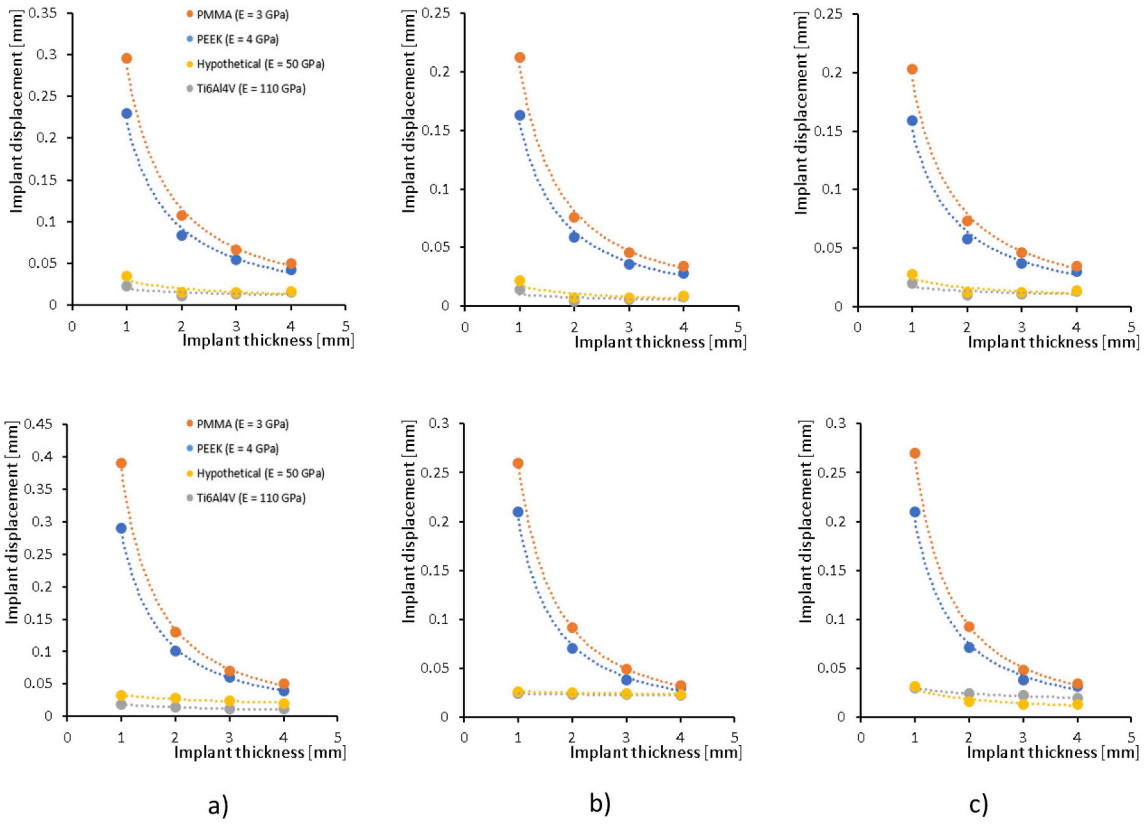

Fig. 8. Coarse model results: Scatter charts represent different loading scenarios: a) ICP + Force, b) ICP + Force(+45), c) ICP + Force(-45); Upper row: Smaller defect (3412 mm^2); Lower row: Larger defect (8030 mm^2). As the Young's modulus of the titanium alloy is significantly higher than that of the two polymer-based materials, the graphs were supplemented by additional results of a hypothetical implant material with a Young's modulus of 50 000 MPa. This offers the possibility of performing a more accurate multiple regression analysis by bridging the gap between the extreme modulus values.

Mises stress in the skull implant was 329 MPa (Ti6Al4V, T1, Smaller defect) and 162 MPa (PEEK, T1, Larger defect). Out of all the configurations, the thinnest PMMA implant configuration resulted in the highest stresses in both the mini-plates (264 MPa, Smaller defect; 200 MPa, Larger defect) and the micro-screws (724 MPa - Smaller defect; 475 MPa - Larger defect). The implant with the lowest stresses was T4, regardless of the material (19–21 MPa, T4, Smaller defect; 22–26 MPa, T4, Larger defect). The thickest titanium alloy implant resulted in the lowest stresses in the mini-plates (50 MPa - Smaller defect; 51 MPa - Larger defect) and micro-screws (60 MPa - Smaller defect; 128 MPa - Larger defect). The maximum von Mises stress values of all 252 configurations were retrieved and reviewed. Typical values observed in the implant, mini-plate and micro-screw for various implant materials and thicknesses are presented in Fig. 10. Results of DOE-based effect assessment are shown in Fig. 11b–d. Effects of all investigated factors and their interactions are represented by dots in Fig. 11b–d. Effects that fall near the line in that figure are considered to be insignificant while those that are far from the line are further tested for statistical significance with ANOVA. Results of the tests are summarized in Tables 4–6.

Table 2
Regression results for UZ displacements.

Load	M	N	Q	R^2	F-value[a]	p-value	Q/N[b]
SMALLER defect[c]							
ICP	14.875	0.543	0.864	0.925	80.4	*< 0.0001*	1.59
ICP + F(45)	25.598	0.647	0.938	0.923	77.7	*< 0.0001*	1.45
ICP + F(-45)	6.040	0.479	0.844	0.908	64.1	*< 0.0001*	1.76
LARGER defect[c]							
ICP	22.217	0.568	0.918	0.920	74.8	*< 0.0001*	1.61
ICP + F(45)	2.196	0.348	0.778	0.761	20.7	*< 0.0001*	2.24
ICP + F(-45)	3.738	0.395	0.971	0.833	32.4	0.0001	2.46

[a] 13° of freedom, $p < 0.05$.
[b] $Q/N_{limit} = 2.60$ for $E_{min} = 3000$ MPa, $E_{max} = 110000$ MPa, $t_{min} = 1$ mm, $t_{max} = 4$ mm ($Q/N_{limit} = 0.21$ for $E_{max} = 4000$ MPa).
[c] Regression coefficients include also results of a hypothetical material performance (E = 50 000 MPa) as described in Fig. 8.

Table 3
ANOVA for UZ displacements.

Source	Sum of squares	Df	Mean square	F-value	p-value
All selected	3.609	5	0.722	134.583	*< 0.0001*
A	2.009	1	2.009	374.569	*< 0.0001*
B	1.007	1	1.007	187.806	*< 0.0001*
C	0.087	1	0.087	16.178	0.0024
AB	0.463	1	0.463	86.312	*< 0.0001*
AC	0.043	1	0.043	8.049	0.0176
Residual	0.054	10	0.003		
Total	3.663	15			

Note: See Fig. 11 for factor (A, B, C etc.) labels.

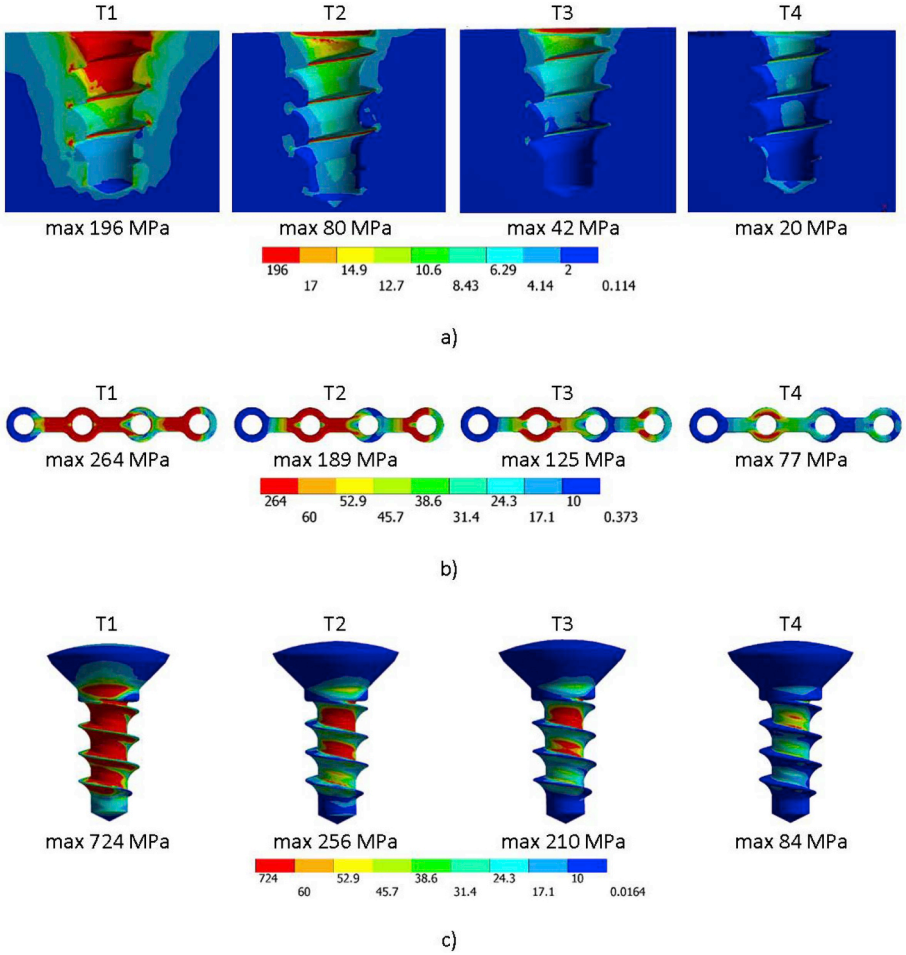

Fig. 9. Typical sub-model results: Von Mises stress distributions in a) PMMA implants (Smaller defect, Position P2, Load Case ICP + Force(+45)), b) mini-plates (Position P2, Load Case ICP + Force(+45)), c) micro-screws fastened in the PMMA implant (Position P2, Load Case ICP + Force(+45)).

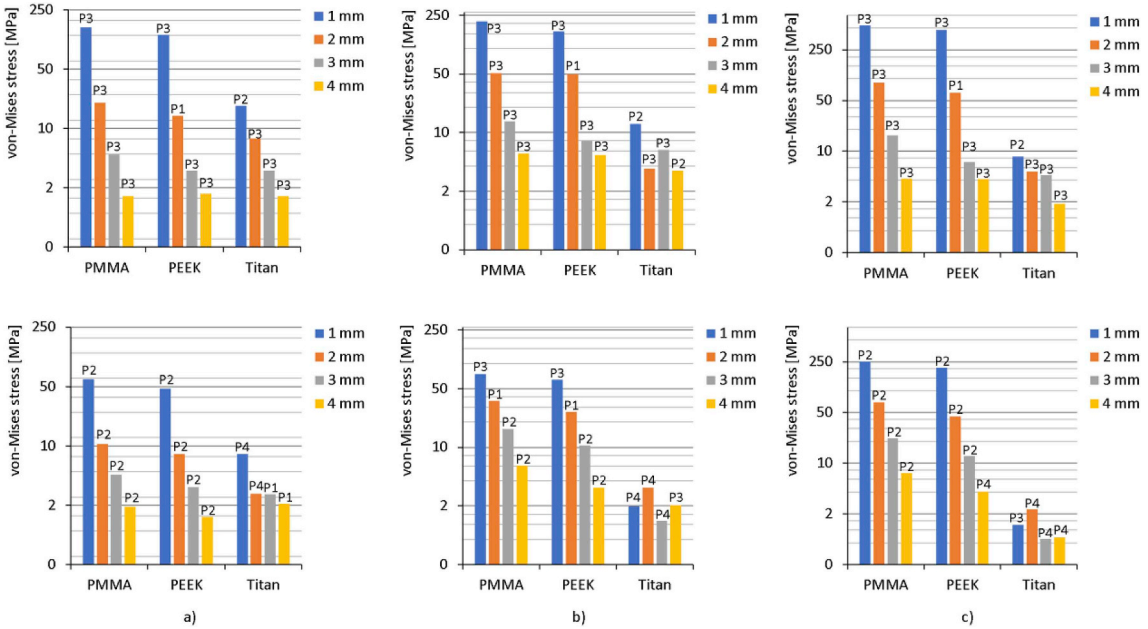

Fig. 10. Typical results of maximum von Mises stress evaluations (results from load case ICP + Force): a) stress in cranial implant, b) stress in mini-plates, c) stress in micro-screw. Upper row: Smaller defect; Lower row: Larger defect.

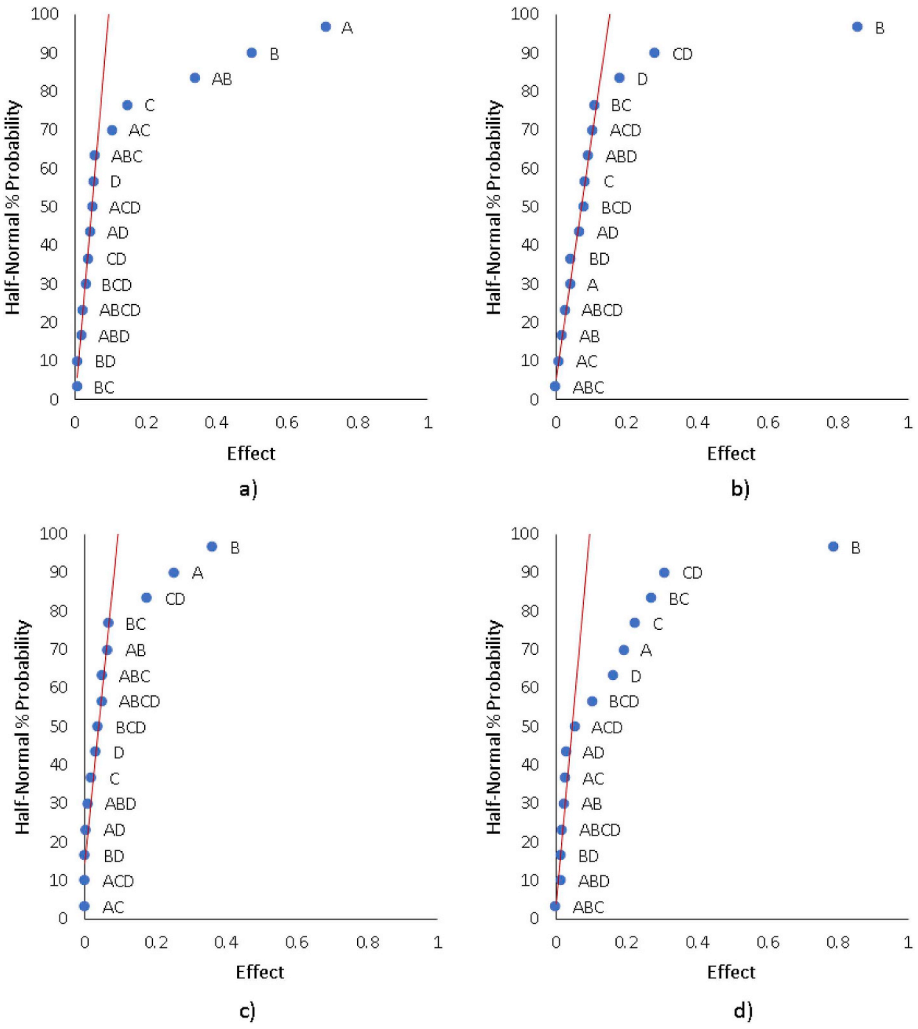

Fig. 11. Half-normal plot of effects of Young's modulus (A), thickness (B), defect size (C), load direction (D) and their interactions (AB, AC, AD … etc.) obtained from DOE-based assessment: a) Implant UZ displacements (from coarse models); b) Implant stress (from sub-models); c) Mini-plate stress (from sub-models); d) Micro-screw stress (from sub-models).

4. Discussion

In the current study, the mechanical performance of two geometrically different cranial implants was assessed. More specifically, global mechanical characteristics such as deformation and mechanical stresses were assessed using different implant thicknesses, implant materials, defect sizes, and loading directions. Since measurements of such mechanical parameters cannot be performed *in vivo* and/or *in vitro* (e.g. measurements of stresses in micro-screw threads and considering a large number of variants), a pure *in silico* approach based on the finite element method was opted for.

To date, most studies, focusing on the analysis of cranial implant models, tend to neglect the complex threaded bone-screw and implant-screw interfaces [12,13,33–35]. Furthermore, in most experimental studies, the interface between the implant and the skull is neglected [36,37]. In the present study, the authors used a sub-modeling approach that included a large number of variants to realistically mimic clinical conditions.

In the first step of the study, 72 coarse models were used to analyse the cranial implant deformation. Transverse deflections of the implants were subsequently evaluated and the results were used to assess the significance of implant material and implant thickness on implant

Table 4
ANOVA for implant stress.

Source	Sum of squares	Df	Mean square	F-value	p-value
All selected	3.379	3	1.126	60.587	*< 0.0001*
B	2.931	1	2.931	157.636	*< 0.0001*
D	0.133	1	0.133	7.163	0.0202
CD	0.315	1	0.315	16.963	0.0014
Residual	0.223	12	0.019		
Total	3.602	15			

Note: See Fig. 11 for factor (B, D, CD) labels.

Table 5
ANOVA for mini-plate stress.

Source	Sum of squares	Df	Mean square	F-value	p-value
All selected	0.919	3	0.306	52.062	*< 0.0001*
A	0.267	1	0.267	45.315	*< 0.0001*
B	0.526	1	0.526	89.351	*< 0.0001*
CD	0.127	1	0.127	21.522	0.0006
Residual	0.071	12	0.006		
Total	0.990	15			

Note: See Fig. 11 for factor (A, B, CD) labels.

Table 6
ANOVA for screw stress.

Source	Sum of squares	Df	Mean square	F-value	p-value
All selected	3.668	7	0.524	177.709	*< 0.0001*
A	0.149	1	0.149	50.662	0.0001
B	2.484	1	2.484	842.392	*< 0.0001*
C	0.202	1	0.202	68.462	*< 0.0001*
D	0.109	1	0.109	36.915	0.0003
BC	0.298	1	0.298	100.911	*< 0.0001*
CD	0.384	1	0.384	130.230	*< 0.0001*
BCD	0.042	1	0.042	14.394	0.0053
Residual	0.024	8	0.003		
Total	3.692	15			

Note: See Fig. 11 for factor (A, B, C etc.) labels.

deflection. For this purpose, two different statistical approaches were used: 1. Multiple linear regression analysis; 2. DOE-based one-way ANOVA. The results acquired using both approaches are summarized in Tables 2 and 3. The results confirmed that the Young's modulus of the implant material and the thickness of the construct significantly affect the implant deflection. Furthermore, the results revealed that the effect of Young's modulus was more significant than that of thickness. Interestingly, when comparing PEEK to PMMA implants (which have very similar values of Young's modulus), the order of significance changes, i.e. in such a case the implant thickness has a more significant effect on the implant deflection than the Young's modulus. Furthermore, the DOE-based one-way ANOVA results revealed that the cranial defect size significantly affects the implant deflection; however, its significance is much lower than that of Young's modulus or thickness.

In the second step of the study, 252 sub-models were analyzed to assess the mechanical stresses in the micro-screws, mini-plates, and cranial implants. The results of von Mises stress confirmed that the critical locations in terms of peak stresses are always situated in the vicinity of the threaded parts. Consequently, the implant-screw interface can be considered one of the most crucial regions regarding the analyses of the implant performance, i.e. neglecting the implant-screw interface in the computational simulations would lead to biased conclusions. As indicated in Fig. 10, the maximum stress magnitudes are similar for both defect sizes. In addition, the peak values of von Mises stresses in all components were used to assess the significance of the implant material, thickness, defect size, and loading direction in terms of mechanical stress. For this purpose, DOE-based one-way ANOVA was used for the assessments; the results are summarized in Tables 4–6 The assessments revealed that in all evaluated cases the implant thickness is the most significant factor affecting the stresses. On the contrary, the implant material represented by the Young's modulus has a lower significance or is even insignificant in terms of effects on the stresses in the evaluated components. Specifically, the effects of thickness on the maximum stress in micro-screw and mini-plate are 2-times and 16-times, respectively, higher than that of Young's modulus. The effect of implant material on the peak stresses in the implant was insignificant. Although the assessment of the limit states (i.e. yielding, fatigue, etc.) was out of scope of this study, it is noteworthy that stress peaks in the thinnest polymer-based implants (T1) regardless the defect size were observed to be quite high (> 80 MPa for PMMA implant, > 127 MPa for PEEK implant). These peak stresses might challenge the yield limits of these materials (approx. 65 MPa and 110 MPa, respectively) leading to a permanent deformation or a failure of the implant. Although this could be remedied by using a titanium alloy for the implant (peak stresses 8 through 329 MPa for T1 depending on load and defect size, yield strength > 800 MPa), a change in implant thickness could be more effective than a change of material in terms of manufacturing costs or dynamic loading resistance.

In the present study, the effects of characteristic design parameters on the implant global mechanical performance during normal functioning were of interest. Therefore, neither manufacturing technology and its impact on the final product (e.g. 3D-printed implant microstructure) nor possible inelasticity of the material were considered in this study as more complex models in terms of material properties would be redundant given the study aims. Despite these limitations, a homogeneous, isotropic and linearly-elastic model was assumed to be a sufficient approximation for the purpose of this study.

5. Conclusion

The detailed models of mini-plates and micro-screws implemented in the finite element simulation provided better insight into the mechanical performance of the implant-skull system. The study provided evidences that increasing implant thickness can be more advantageous than changing the implant material in terms of maximum von Mises stress in all investigated components. However, when a change of implant deflection is required, it should be considered that implant material has slightly higher effect on the change than implant thickness. These observations might affect the surgeons' decision-making process when designing and manufacturing of cranial implants.

Acknowledgement

The work was supported by the Czech Science Foundation by Grant No. 16-08944S.

Appendix

It is assumed that transversal displacements of cranial implant are negatively correlated to the Young's modulus and thickness of the implant. This assumption is based on the conclusions of the classical Kirchhoff Plate Theory [38]. Pursuant this theory, thin and flat plates under transverse loading deflect according to the following formula:

$$\nabla^2\nabla^2 w = -\frac{12(1-\mu^2)q}{Et^3} \tag{A.1}$$

where w is transverse deflection (labeled as UZ throughout this paper), E is Young's modulus, q is transverse load, μ is Poisson's number and t is the plate thickness. In a specific case of thin and flat circular plate with the radius R, loaded by a concentrated load P in the center and fixed in axial direction on its edge, the following formula for the maximum transverse displacement can be derived from Eq. (A.1) [39]:

$$w = -0.239 \cdot \frac{PR^2(1-\mu)(3+\mu)}{Et^3} \tag{A.2}$$

Maximum displacement of a thin, flat and circular plate following Eq. (A2) decreases when the plate thickness increases; this dependency is described by a cubic curve as indicated in the formula by the thickness exponent of 3. Similarly, deflection changes inversely to E (exponent of 1 in the denominator of Eq. (A.2)).

In the case of a partially-spherical shell with a load P concentrated on a small area, the maximum deflection can be obtained using the following

formula [39]:

$$w = -A\frac{PR\sqrt{1-\mu^2}}{Et^2} \tag{A.3}$$

where R is a radius of the curvature of the partially-spherical shell and A is a tabulated numerical coefficient that depends upon specifics of the model. Eq. (A.3) again indicates that the maximum displacement decreases when the plate thickness increases wherein the dependency is described by a quadratic curve (note the thickness exponent of 2 in Eq. 3). It is also noteworthy that while the negative correlation of w on E and t remains, the exponents of the power functions change (3 → 2); thus, the interaction of E and t changes as well.

A geometrical resemblance between an ideal partially-spherical shell and a cranial implant is obvious. Therefore, the negative correlation of w on E and t can still be expected; however, the interaction of E and t as well as their specific effect on cranial displacement cannot be determined using exact formulas such as those discussed above. Nevertheless, an approximation based on considerations of this Appendix can be derived using FEM results.

Conflicts of interest

None declared.

Author contributions statements

PM, NN and LB wrote the main manuscript. JW supervising. PM, LB and JCH performed FEA. All authors reviewed the manuscript.

References

[1] S.V. Murphy, A. Atala, 3D bioprinting of tissues and organs, Nat. Biotechnol. 32 (2014) 773–785, https://doi.org/10.1038/nbt.2958.

[2] M.K. Alibhai, I. Balasundaram, C. Bridle, S.B. Holmes, Is there a therapeutic role for cranioplasty? Int. J. Oral Maxillofac. Surg. 42 (2013) 559–561, https://doi.org/10.1016/j.ijom.2013.01.001.

[3] J.W. Stansbury, M.J. Idacavage, 3D printing with polymers: challenges among expanding options and opportunities, Dent. Mater. 32 (2016) 54–64, https://doi.org/10.1016/j.dental.2015.09.018.

[4] The Lancet, How can registries and innovation improve surgical care? Lancet 388 (2016) 1349, https://doi.org/10.1016/S0140-6736(16)31763-9.

[5] M.V.M. Anchieta, F.A. Salles, B.D. Cassaro, M.M. Quaresma, B.F.O. Santos, Skull reconstruction after resection of bone tumors in a single surgical time by the association of the techniques of rapid prototyping and surgical navigation, Int. J. Comput. Assist. Radiol. Surg. 11 (2016) 1919–1925, https://doi.org/10.1007/s11548-016-1415-2.

[6] T. Zegers, M. Ter Laak-Poort, D. Koper, B. Lethaus, P. Kessler, The therapeutic effect of patient-specific implants in cranioplasty, J. Cranio-Maxillo-Fac. Surg. 45 (2017) 82–86, https://doi.org/10.1016/j.jcms.2016.10.016.

[7] K. Moiduddin, S. Darwish, A. Al-Ahmari, S. ElWatidy, A. Mohammad, W. Ameen, Structural and mechanical characterization of custom design cranial implant created using additive manufacturing, Electron. J. Biotechnol. 29 (2017) 22–31, https://doi.org/10.1016/j.ejbt.2017.06.005.

[8] F. Chana-Rodríguez, R.P. Mañanes, J. Rojo-Manaute, P. Gil, J.M. Martínez-Gómiz, J. Vaquero-Martín, 3D surgical printing and pre contoured plates for acetabular fractures, Injury 47 (2016) 2507–2511, https://doi.org/10.1016/j.injury.2016.08.027.

[9] D.O. Visscher, E. Farré-Guasch, M.N. Helder, S. Gibbs, T. Forouzanfar, P.P. van Zuijlen, J. Wolff, Advances in bioprinting technologies for craniofacial reconstruction, Trends Biotechnol. 34 (2016) 700–710, https://doi.org/10.1016/j.tibtech.2016.04.001.

[10] A. Ridwan-Pramana, P. Marcian, L. Borak, N. Narra, T. Forouzanfar, J. Wolff, Finite element analysis of 6 large PMMA skull reconstructions: a multi-criteria evaluation approach, PLoS One 12 (2017), https://doi.org/10.1371/journal.pone.0179325.

[11] A. Ridwan-Pramana, P. Marcián, L. Borák, N. Narra, T. Forouzanfar, J. Wolff, Structural and mechanical implications of PMMA implant shape and interface geometry in cranioplasty - a finite element study, J. Cranio-Maxillofacial Surg. 44 (2016), https://doi.org/10.1016/j.jcms.2015.10.014.

[12] V.P. Bogu, Y.R. Kumar, A. Kumar Khanara, Modelling and structural analysis of skull/cranial implant: beyond mid-line deformities, Acta Bioeng. Biomech. 19 (2017) 125–131 http://www.ncbi.nlm.nih.gov/pubmed/28552926.

[13] V. Phanindra Bogu, Y. Ravi Kumar, A. Kumar Khanra, Homogenous scaffold-based cranial/skull implant modelling and structural analysis—unit cell algorithm-meshless approach, Med. Biol. Eng. Comput. 55 (2017) 2053–2065, https://doi.org/10.1007/s11517-017-1649-3.

[14] J. Chamrad, P. Marcián, N. Narra, L. Borák, Evaluating different shapes of cranial fixation mini-plates using finite element method, IFMBE Proc, 2017, https://doi.org/10.1007/978-981-10-5122-7_187.

[15] D. Garcia-Gonzalez, J. Jayamohan, S.N. Sotiropoulos, S.-H. Yoon, J. Cook, C.R. Siviour, A. Arias, A. Jérusalem, On the mechanical behaviour of PEEK and HA cranial implants under impact loading, J. Mech. Behav. Biomed. Mater. 69 (2017) 342–354, https://doi.org/10.1016/j.jmbbm.2017.01.012.

[16] B.A. Khader, M.R. Towler, Materials and techniques used in cranioplasty fixation: a review, Mater. Sci. Eng. C 66 (2016) 315–322, https://doi.org/10.1016/j.msec.2016.04.101.

[17] B. Lethaus, M. Bloebaum, B. Essers, M.P. ter Laak, T. Steiner, P. Kessler, Patient-specific implants compared with stored bone grafts for patients with interval cranioplasty, J. Craniofac. Surg. 25 (2014) 206–209, https://doi.org/10.1097/SCS.0000000000000396.

[18] J. Chamrad, P. Marcián, L. Borák, On the level of computational model of a human skull: a comparative study, Appl. Comput. Mech. 12 (2018), https://doi.org/10.24132/acm.2018.385.

[19] P. Marcián, O. Konečný, L. Borák, J. Valášek, K. Řehák, D. Krpalek, Z. Florian, On the Level of Computational Models in Biomechanics Depending on Gained Data from CT/MRI and Micro-CT, Mendel, 2011.

[20] M. Freedman, M. Ring, L.F.A. Stassen, Effect of alveolar bone support on zygomatic implants in an extra-sinus position–a finite element analysis study, Int. J. Oral Maxillofac. Surg. 44 (2015) 785–790, https://doi.org/10.1016/j.ijom.2015.01.009.

[21] J.A. Motherway, P. Verschueren, G. Van der Perre, J. Vander Sloten, M.D. Gilchrist, The mechanical properties of cranial bone: the effect of loading rate and cranial sampling position, J. Biomech. 42 (2009) 2129–2135, https://doi.org/10.1016/j.jbiomech.2009.05.030.

[22] T. Preusser, M. Rumpf, S. Sauter, L.O. Schwen, 3D composite finite elements for elliptic boundary value problems with discontinuous coefficients, SIAM J. Sci. Comput. 33 (2011) 2115–2143, https://doi.org/10.1137/100791750.

[23] F.J. Gómez, M. Elices, Fracture of components with V-shaped notches, Eng. Fract. Mech. 70 (2003) 1913–1927, https://doi.org/10.1016/S0013-7944(03)00131-0.

[24] J. Pellier, J. Geringer, B. Forest, Fretting-corrosion between 316L SS and PMMA: influence of ionic strength, protein and electrochemical conditions on material wear. Application to orthopaedic implants, Wear 271 (2011) 1563–1571, https://doi.org/10.1016/j.wear.2011.01.082.

[25] M. Niinomi, Mechanical properties of biomedical titanium alloys, Mater. Sci. Eng. 243 (1998) 231–236, https://doi.org/10.1016/S0921-5093(97)00806-X.

[26] F. Chen, S. Gatea, H. Ou, B. Lu, H. Long, Fracture characteristics of PEEK at various stress triaxialities, J. Mech. Behav. Biomed. Mater. 64 (2016) 173–186, https://doi.org/10.1016/j.jmbbm.2016.07.027.

[27] M. Czosnyka, Monitoring and interpretation of intracranial pressure, J. Neurol. Neurosurg. Psychiatry 75 (2004) 813–821, https://doi.org/10.1136/jnnp.2003.033126.

[28] N. Yoganandan, F.A. Pintar, J. Zhang, J.L. Baisden, Physical properties of the human head: mass, center of gravity and moment of inertia, J. Biomech. 42 (2009) 1177–1192, https://doi.org/10.1016/j.jbiomech.2009.03.029.

[29] K. Akça, A. Eser, S. Canay, Numerical simulation of the effect of time-to-loading on peri-implant bone, Med. Eng. Phys. 32 (2010) 7–13, https://doi.org/10.1016/j.medengphy.2009.10.001.

[30] H.-L. Liu, C.-L. Lin, M.-T. Sun, Y.-H. Chang, Numerical investigation of macro- and micro-mechanics of a ceramic veneer bonded with various cement thicknesses using the typical and submodeling finite element approaches, J. Dent. 37 (2009) 141–148, https://doi.org/10.1016/j.jdent.2008.10.009.

[31] J.E. Johnson, K.L. Troy, Validation of a new multiscale finite element analysis approach at the distal radius, Med. Eng. Phys. 44 (2017) 16–24, https://doi.org/10.1016/j.medengphy.2017.03.005.

[32] C. Rungsiyakull, J. Chen, P. Rungsiyakull, W. Li, M. Swain, Q. Li, Bone's responses to different designs of implant-supported fixed partial dentures, Biomechanics Model. Mechanobiol. 14 (2015) 403–411, https://doi.org/10.1007/s10237-014-0612-6.

[33] A. Tsouknidas, S. Maropoulos, S. Savvakis, N. Michailidis, FEM assisted evaluation of PMMA and Ti6Al4V as materials for cranioplasty resulting mechanical behaviour and the neurocranial protection, Bio Med. Mater. Eng. 21 (2011) 139–147, https://doi.org/10.3233/BME-2011-0663.

[34] J. Persson, B. Helgason, H. Engqvist, S.J. Ferguson, C. Persson, Stiffness and strength of cranioplastic implant systems in comparison to cranial bone, J. Cranio-

Maxillofacial Surg. 46 (2018) 418–423, https://doi.org/10.1016/j.jcms.2017.11.025.
[35] F. El Halabi, J.F. Rodriguez, L. Rebolledo, E. Hurtós, M. Doblaré, Mechanical characterization and numerical simulation of polyether–ether–ketone (PEEK) cranial implants, J. Mech. Behav. Biomed. Mater. 4 (2011) 1819–1832, https://doi.org/10.1016/j.jmbbm.2011.05.039.
[36] G. Ambrogio, G. Palumbo, E. Sgambitterra, P. Guglielmi, A. Piccininni, L. De Napoli, T. Villa, G. Fragomeni, Experimental investigation of the mechanical performances of titanium cranial prostheses manufactured by super plastic forming and single-point incremental forming, Int. J. Adv. Manuf. Technol. (2018), https://doi.org/10.1007/s00170-018-2338-6.
[37] S. Berretta, K. Evans, O. Ghita, Additive manufacture of PEEK cranial implants: manufacturing considerations versus accuracy and mechanical performance, Mater. Des. 139 (2018) 141–152, https://doi.org/10.1016/j.matdes.2017.10.078.
[38] O.A. Bauchau, J.I. Craig (Eds.), Structural Analysis, Springer Netherlands, Dordrecht, 2009, , https://doi.org/10.1007/978-90-481-2516-6.
[39] W. Young, R. Budynas, Roark's Formulas for Stress and Strain, 7 edition, McGraw-Hill Professional, 2001.